Variability of the blazar S5 1803+784 in July 2019 - December 2024 as a manifestation of the jet flow structure

M. Butuzova · M. Gorbachev · V. Guseva · A. Krivenko · S. Nazarov · G. Baida

Crimean Astrophysical Observatory of the Russian Academy of Sciences,
Nauchny, 298409 Russia

DOI: 10.26119/2025-moc02 EDN: wzqnfr
eLocator: moc02

Abstract. The TESS satellite provides unique data from nearly continuous observations with high temporal resolution. Each sky sector is observed for 27 days. For the blazar S5 1803+784, there are three observing seasons during which the object remains in the TESS field of view for extended periods, approximately 10 months in total. By supplementing these data with multi-band photometric observations from the Zwicky Transient Facility (ZTF) and the AZT-8 telescope at the Crimean Astrophysical Observatory of the Russian Academy of Sciences, we obtain a unique opportunity to study the relation between the shortest characteristic variability timescales and the parameters of long-term variability. Based on this analysis, we conclude that short-term variability is caused by the emergence and evolution of jet regions, whose motion deviates from the general trajectory, and, therefore, they have different Doppler factors. We performed light curve modeling under this assumption and obtained good qualitative agreement with the observations.

Keywords: active galaxies: blazars; optical variability

1. Introduction

Blazars exhibit prominent variability on timescales ranging from several hours to several years. Variability on timescales of several days has been poorly studied due to limitations imposed by Earth's diurnal rotation and weather conditions, which prevent continuous data collection over multiple days at a single observatory. To address this, international observational campaigns have previously been performed, such as the Whole Earth Blazar Telescope (WEBT). The situation has changed with the launch of the Transiting Exoplanet Survey Satellite (TESS). TESS observes a $24^\circ \times 96^\circ$ patch of the sky for 27 days (one sector) with a time resolution of 2 to 30 minutes. Afterwards, the observed field is shifted. Regions near the ecliptic poles are observed most frequently, allowing objects in these areas to accumulate long, nearly continuous light curves spanning several months to a year. We used such a unique dataset to study the blazar S5 1803+784. In Section 2, we describe the method used to construct the blazar's light curve from TESS data, taking into account the object's low brightness and the characteristics of TESS's CCD detectors. Section 3 presents the results of our analysis of the evolution of the shortest characteristic variability timescale (τ), and the search for possible correlations between τ and photometric variability properties as well as the spectral index α (defined as $F \propto \nu^{\alpha}$). Section 4 contains the results of light curve modeling under the assumption that the internal flow structure is responsible for the formation of variability on a short time scale. Discussion and conclusions are presented in Section 5.

2. Data

TESS provides three types of data products: SAP and PDCSAP light curves, and Full Frame Images (FFIs). SAP light curves account only for background subtraction. PDCSAP light curves include corrections for instrumental systematics and the overall field trend. Some authors (Weaver et al. 2020; Raiteri et al. 2021a,b) note that only SAP light curves are suitable for studying blazars, as they correspond to light curves obtained with ground-based telescopes, while the PDCSAP light curves remove long-term trends of astrophysical origin.

Since blazars are faint sources, both their SAP and PDCSAP light curves are strongly affected by Poisson noise, which distorts analyses of temporal variability properties (Butuzova et al. 2025; Gorbachev & Butuzova 2025). To reduce the noise component, we performed relative photometry of the blazar using cuts from the full-frame images, following the method proposed by Butuzova et al. (2025). The exposure time per image varied across TESS sectors; therefore, the number of cuts used for co-addition was varied and determined empirically to achieve a photometric precision better than 0.02 magnitudes. The comparison stars used in our analysis are listed in Table 1. Resulting TESS light curves are obtained for magnitudes.

One of the characteristics of TESS data is the variation in the zero point of the instrumental flux between different sectors. Additionally, we found that even within the same CCD chip, this zero point changes in an uncorrelated manner between adjacent sectors (Fig. 1). To demonstrate this effect, we selected sector 14 as a reference and identified several sources with no significant intrinsic variability that were observed in sectors 14, 15, and 16 on the same CCD chip. For each selected source, we computed the median SAP flux in each sector, and then calculated the difference between the median fluxes in sectors 15 and 16 relative to sector 14: $\Delta F^i = F^{14}_{\rm median} - F^i_{\rm median}$, where i is the sector index. We then normalized the data in each sector by subtracting the median flux values. To account for zero-point shifts, the corresponding ΔF^i value was added to the normalized fluxes in sectors 15 and 16.

Differences in CCD chip sensitivity must be taken into account when constructing a combined light curve of an object over multiple sectors. To do this, we used a combined ground-based light curve as a reference, constructed as follows. We matched the R-band photometry from the AZT-8 telescope to the g-band ZTF light curve for two observation seasons 2022 and 2024, for which AZT-8 data are available. For each observing intervals, we shifted the R-band light curve relative

Table 1. Stars used in the photometry of the S5 1803+784 blazar conducted for FFI cuts.

Star	R.A.	Dec.	TESS magnitude
TIC 288430540	269.83017	+78.50756	13.78
TIC 288432310	269.98167	+78.44307	13.82
TIC 288432315	270.40571	+78.44980	15.63
TIC 288432354	270.10727	+78.54506	15.66

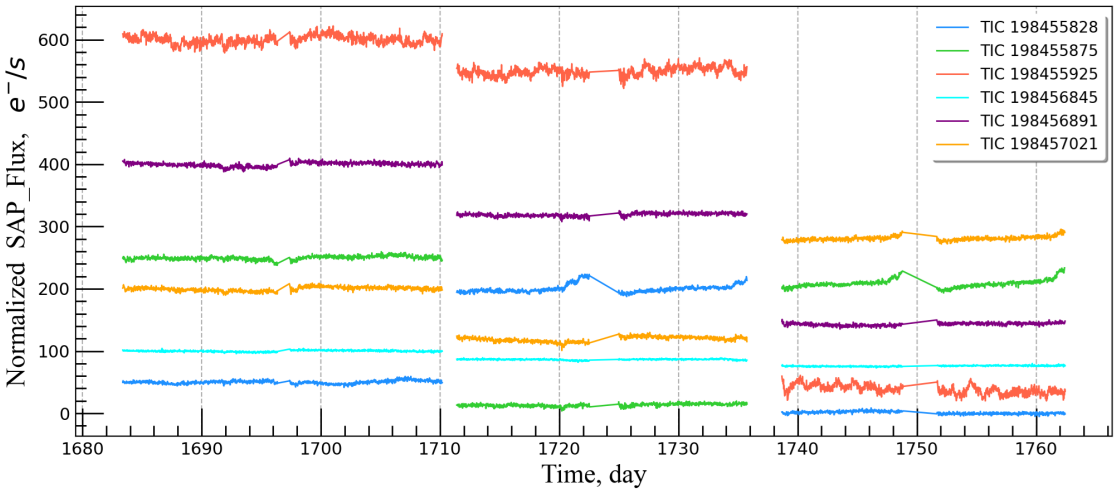

Figure 1. The change in the instrumental flux of six stars falling on one CCD in the period from sector 14 to 16. For ease of comparison, the data from different sources are presented with a vertical offset relative to each other.

to the g-band in such a way that the sum of squared differences between the R-band data points and the linear interpolation between the two nearest g-band points at the corresponding R-band epochs was minimized. The derived offsets were 0.72 and 0.67 magnitudes for 2022 and 2024, respectively.

Similarly, each continuous segment of the TESS light curve was aligned with the combined ground-based light curve of ZTF and AZT-8. However, some intervals of uniformly sampled TESS data lacked corresponding g- and R-band measurements or contained only a very small number of such points. For these segments, the vertical offset of the TESS light curve was determined by matching the flux levels at the edges with adjacent segments. These segments were excluded from further analysis. As for example, the final combined light curve is presented in the left panel of Fig. 2. Right panel shows obtained TESS light curves for observed seasons 2019-2020 (top) and 2024 (bottom).

Using ZTF and AZT-8 data, we calculated the spectral index following the method described by Gorbachev et al. (2024). The spectral indices derived from ZTF data are statistically lower than those based on AZT-8 data. We attribute this difference to the fact that AZT-8 observations were performed simultaneously in four photometric bands, whereas ZTF provides quasi-simultaneous observations (separated by one to two days) in two bands, and rarely in three, for the blazar S5 1803+784. On the basis of the ZTF data, we constructed a combined spectral index evolution curve using the same method applied to the light curves.

Due to data gaps within each TESS sector, a single continuous data segment spans only about ten days. The blazar S5 1803+784 was observed over three seasons, each consisting of several consecutive TESS sectors, sometimes separated by a gap of one or two sectors (Fig. 2). Each of these seasons (July 19, 2019 – June 8, 2020; December 31, 2021 – January 18, 2023;

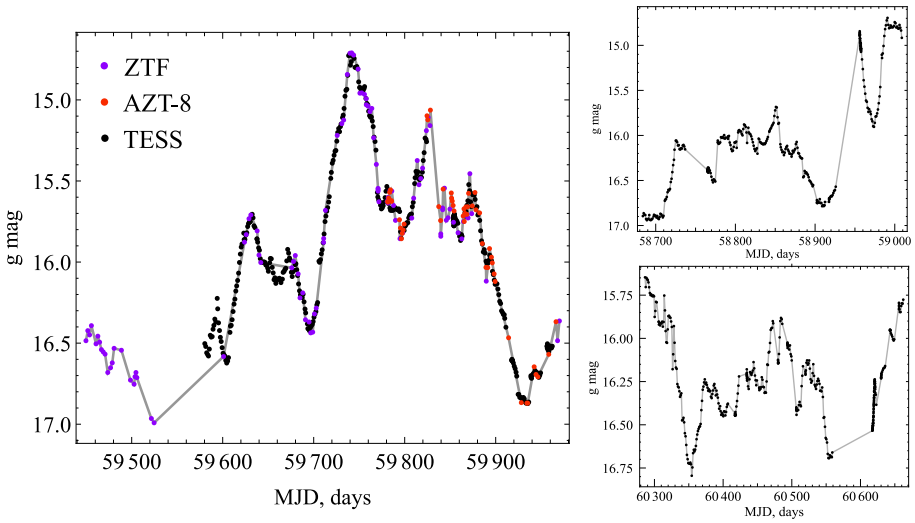

Figure 2. The light curves of the blazar S5 1803+784 for the period from 02.05.2019 to 13.07.2020 (right top), from 22.08.2021 to 21.01.2023 (left), and from 12.10.2023 to 20.12.2024 (right bottom).

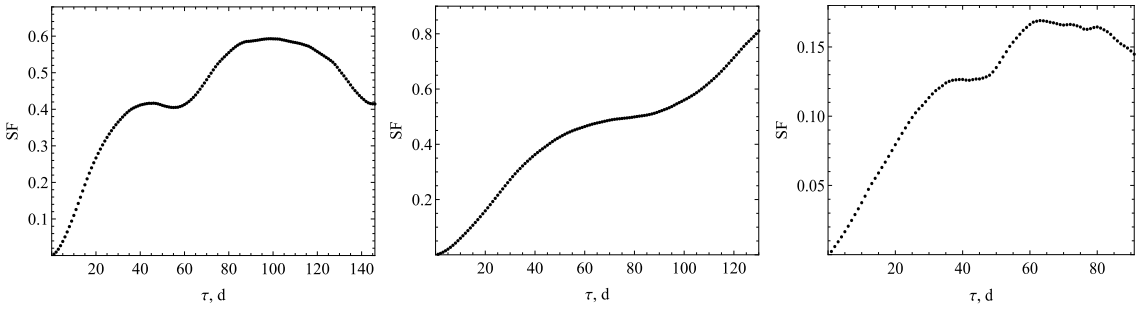

Figure 3. Structure functions for the three observation seasons of the blazar S5 1803+784. The maximum value along the abscissa axis is one third of the duration of the interval for which the corresponding SF is calculated.

and December 7, 2023 – December 18, 2024) covers approximately one year of high-cadence observations. These data are unique and enable the study of correlations between blazar flux variability properties on different timescales (Table 2). The fact that S5 1803+784 exhibited different mean brightness, variability amplitude, and characteristic variability timescale during each season (see Section 3) allows us to analyze the relationship between the shortest characteristic variability timescale and the photometric parameters of long-term variability, to identify the physical mechanisms driving variability at different timescales.

3. Relation of temporal and photometric variability properties

Since the blazar variability has a stochastic character, we consider it enough to find the characteristic variability time τ as the time interval during which it is possible to register an object's brightness change in both directions. Thus, τ is the position of the maximum of the structure function (SF) defined by Simonetti et al. (1985). In this case, the peak value of SF represents the square of the average variability amplitude within the considered time interval. To determine τ for observation intervals for almost a year, we used a combined light curve in the g, R, and TESS bands (Fig. 2), in which the TESS data were averaged over one day. Then, for data points evenly spaced for one day, we determined the magnitudes using linear interpolation between two adjacent data points. Then we calculated SF (Fig. 3) and obtained τ (Table 2).

Table 2. Characteristics of the long-term variability of the S5 1803+784 blazar.

Interval	designation in the text	median magnitude	amplitude	median spectral index	characteristic time of variability, d
07.2019 – 06.2020	2019	16.5	2.36	−1.68	43.0 and 93.3
12.2021 – 01.2023	2022	15.91	2.16	−1.64	76.4
12.2023 – 12.2024	2024	16.26	1.14	−1.56	33.9 and 64.3

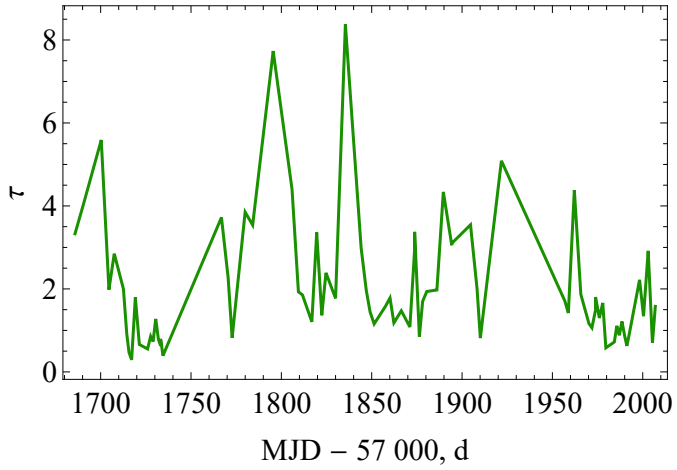

Figure 4. The evolution of the shortest characteristic time of variability for the period from 05.2019 to 07.2020.

On short time scales, variability occurs with smaller amplitude, so its characteristic time does not manifest in SF computed from data over long time intervals. Additionally, the characteristics of the process responsible for short-term variability may change over time, or the process itself may be replaced by another one. This leads to variations in τ of short-term variability. To determine τ, we used the method proposed by Butuzova et al. (2025), which involves adding data points to a short time series until a statistically significant maximum (at the 0.95 confidence level) appears in SF. The next consecutive short time series is then selected, and the procedure is repeated. This method was applied to segments of continuous, uniformly sampled TESS data. Figure 4 shows the evolution of the characteristic variability timescale from May 2019 to July 2020. It can be seen that τ varies by a factor of several times between neighboring time intervals.

For each interval with a determined τ, we calculated the average variability amplitude ($\overline{\text{var ampl}}$), the mean magnitude ($< \text{mag} >$), the maximum brightness variation (Δmag), and the spectral index. Figure 5 shows the relations between these parameters. The absence of a dependence between Δmag and τ indicates that long-term trends do not significantly affect variability on short timescales.

Blazar brightness variability is caused either by physical changes within the jet — such as the passage of a shock (Marscher & Gear 1985) — or by variations in the relativistic boosting factor (Doppler factor) due to changes in the jet's speed and/or direction relative to the observer. On short timescales, flux variations may arise, for example, from turbulent cells passing through a shock front (TEMZ model, Marscher (2025)). Alternatively, inhomogeneities and instabilities in the jet flow may give rise to regions (subcomponents) moving at some angle relative to the general jet trajectory, thereby resulting in a different Doppler factor. The continuous emergence and evolution of such subcomponents lead to variability characterized by a changing color index behavior with brightness (Butuzova 2021; Gorbachev et al. 2022), whereas physical changes within the jet would typically produce a clear dependence of the color index with brightness. Figure 5f shows no such dependence across all data under consideration.

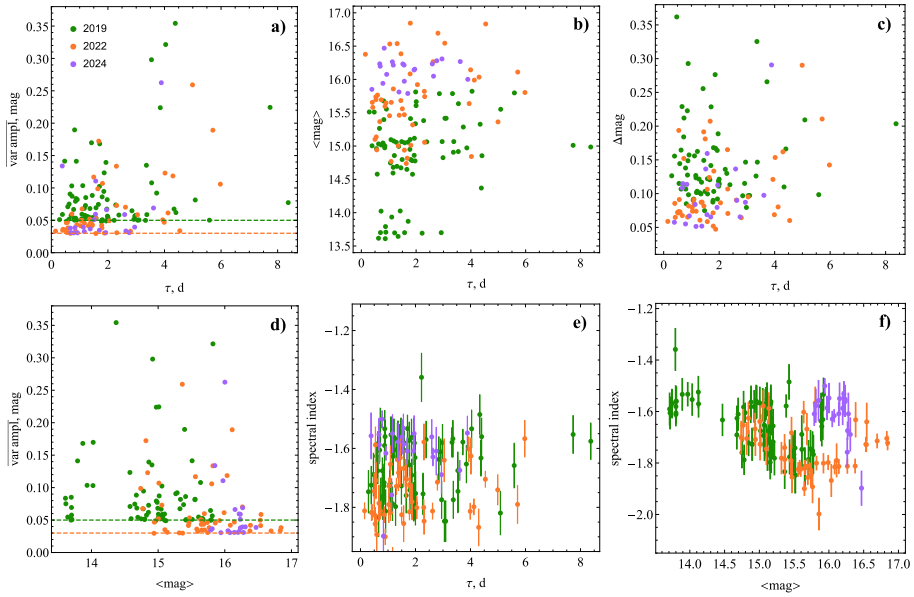

Figure 5. The correlation between photometric and temporal characteristics of the variability of the S5 1803+784 on various time scales. The dotted line on graphs ***a*** and ***d*** indicates the minimum value of the average amplitude of variability from which the calculation of the significance level of the SF peak begins when searching for the shortest characteristic time of variability.

Notably, the range of τ values does not depend on the spectral index (Fig. 5e) and remains approximately constant across all three observing seasons, during which the source exhibited different brightness levels (Fig. 5b). If the variability was driven by physical changes in the jet, this behavior would require an implausibly fine-tuned adjustment of parameters.

On the other hand, if long-term variability was caused by changes in the Doppler factor, then τ would decrease with increasing brightness. This trend is not observed (Fig. 5a), and its absence can be explained by the fact that subcomponents have different sizes (Butuzova 2021; Butuzova et al. 2025). If all subcomponents had the same size but different Doppler factors, the average variability amplitude would be larger for smaller τ values. Conversely, if the Doppler factors were the same but the sizes varied, the relation would be inverse. Furthermore, the continuous action of a single physical process driving short-term variability throughout all observing seasons is supported by the fact that the distribution of τ values follows a log-normal distribution with $\mu = 0.43$ and $\sigma = 0.75$ (Pearson $\chi^2 = 0.55$; Fig. 6).

4. Modeling of the light curve

We performed light curve simulations under the assumption that variability arises from subcomponents within the jet. To do this, we applied the formulas from (Butuzova 2021) to the geometric configuration described in (Gorbachev & Butuzova 2025). Specifically, we modeled the optical-emitting region as a cylinder with a length of $5 \cdot 10^{-2}$ pc and a radius of $5 \cdot 10^{-4}$ pc. Subcomponents appear randomly in time and location within this region, each moving along a helical trajectory on the surface of a cone with a half-opening angle $\chi \leqslant 4°$. The cone's axis coincides with the jet axis and is oriented at an angle of 5° to the line of sight. The angle between the cone generatrix and the subcomponent's velocity vector ranges from 1° to 10°. The velocities of both the jet and subcomponents are assumed to be $0.99c$, where c is the speed of light. The total volume of simultaneously existing subcomponents does not exceed 30% of the emitting region's volume. The flux of the non-variable component in the observer's frame is 1 mJy.

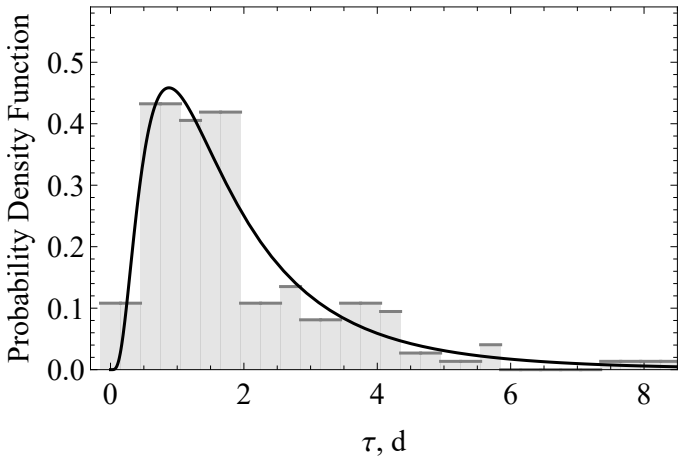

Figure 6. The probability density for τ and its fitting by a log-normal distribution.

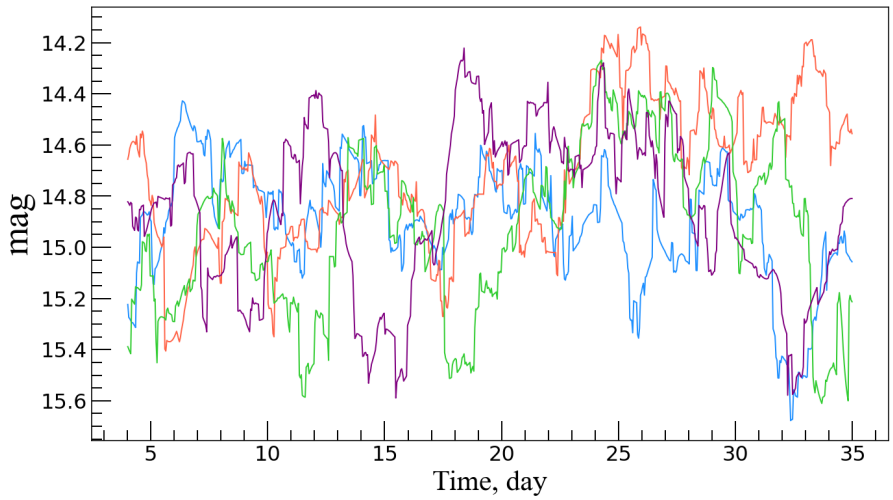

Figure 7. Light curves generated under the assumption of the appearance and evolution of subcomponents in the jet flow moving along a helical line relative to the axis of the emitting region. The different colors correspond to different realizations of the model's light curves.

Figure 7 shows a qualitatively good agreement between the simulated and observed light curves of the blazar S5 1803+784, namely, there are alternating individual sharp-peak flares. Importantly, the azimuthal angle of each subcomponent changes by only a few degrees during its passage through the emitting region. Therefore, the flares seen in the model light curves (Fig. 7) arise from the superposition of emission from multiple subcomponents, rather than from the rotation of a single subcomponent around the jet axis.

5. Summary

Over the observed period, the brightness of the blazar S5 1803+784 varied from 16.9 to 14.7 magnitudes in the g-band, while the spectral index ranged from -2.0 to -1.36. The long-term variability is achromatic.

The shortest characteristic variability timescale ranges from 0.2 to 8.5 days and changes irregularly between adjacent time intervals on the light curve, sometimes by factor of several times. The distribution of τ follows a log-normal law with $\mu = 0.43$ and $\sigma = 0.75$. This, together with the

absence of correlations between τ and both short-term (variability amplitude) and long-term (mean brightness, spectral index) photometric parameters, suggests that the short-timescale variability arises from the emergence and evolution of subcomponents—regions within the jet flow that move at an angle relative to the overall jet trajectory. Light curve simulations based on this assumption show good qualitative agreement with the observed light curves.

Acknowledgements This paper includes data collected by the TESS missions and obtained from the MAST data archive at the Space Telescope Science Institute (STScI). Funding for the TESS mission is provided by the NASA Explorer Program.

Based on observations obtained with the Samuel Oschin Telescope 48-inch and the 60-inch Telescope at the Palomar Observatory as part of the Zwicky Transient Facility project.

Funding

This work was supported by the Russian Science Foundation, No. 24-22-00343.

References

Butuzova M.S., Guseva V.A., Gorbachev M.A., et al., 2025, Journal of High Energy Astrophysics, 45, p. 19
Butuzova M.S., 2021, Astroparticle Physics, 129, id. 102577
Gorbachev M.A. and Butuzova M.S., 2025, Astronomical and Astrophysical Transactions, in press
Gorbachev M.A., Butuzova M.S., Nazarov S.V., et al., 2024, Astroparticle Physics, 160, id. 102965
Gorbachev M.A., Butuzova M.S., Sergeev S.G., et al., 2022, Astrophysical Journal, 928, 1, p. 86
Marscher A.P. and Gear W.K., 1985, Astrophysical Journal, 298, p. 114
Marscher A.P., 2014, Astrophysical Journal, 780, 1, p. 87
Raiteri C.M., Villata M., Carosati D., et al., 2021a, Monthly Notices of the Royal Astronomical Society, 501, 1, p. 1100
Raiteri C.M., Villata M., Larionov V.M., et al., 2021b, Monthly Notices of the Royal Astronomical Society, 504, 4, p. 5629
Simonetti J.H., Cordes J.M., Heeschen D.S., 1985, Astrophysical Journal, 296, p. 46
Weaver Z.R., Williamson K.E., Jorstad S.G., et al., 2020, Astrophysical Journal, 900, 2, p. 137